

Identifying multi-stage nanocrystal growth using in situ TEM video data

YanJun Qian, Jianhua Z. Huang & Yu Ding

To cite this article: YanJun Qian, Jianhua Z. Huang & Yu Ding (2017) Identifying multi-stage nanocrystal growth using in situ TEM video data, IISE Transactions, 49:5, 532-543, DOI: [10.1080/24725854.2016.1251666](https://doi.org/10.1080/24725854.2016.1251666)

To link to this article: <http://dx.doi.org/10.1080/24725854.2016.1251666>



Accepted author version posted online: 26 Oct 2016.
Published online: 26 Oct 2016.



[Submit your article to this journal](#)



Article views: 107



[View related articles](#)



[View Crossmark data](#)

Identifying multi-stage nanocrystal growth using in situ TEM video data

YanJun Qian^a, Jianhua Z. Huang^b and Yu Ding^a

^aDepartment of Industrial & System Engineering, Texas A&M University, College Station, TX, USA; ^bDepartment of Statistics, Texas A&M University, College Station, TX, USA

ABSTRACT

The in situ transmission electron microscopy technique is receiving considerable attention in material science research, as its in situ nature makes possible discoveries that ex situ instruments are unable to make and provides the capability of directly observing nanocrystal growth processes. As increasing amounts of dynamic transmission electron microscopy (TEM) video data become available, one of the bottlenecks appears to be the lack of automated, quantitative, and dynamic analytic tools that can process the video data efficiently. The current processing is largely manual in nature and thus laborious, with existing tools focusing primarily on static TEM images. The absence of automated processing of TEM videos does not come as a surprise, as the growth of nanocrystals is highly stochastic and goes through multiple stages. We introduce a method in this article that is suitable for analyzing the in situ TEM videos in an automated and effective way. The method learns and tracks the normalized particle size distribution and identifies the phase-change points delineating the stages in nanocrystal growth. Using the outcome of the change-point detection process, we propose a hybrid multi-stage growth model and test it on an in situ TEM video, made available in 2009 by *Science*.

ARTICLE HISTORY

Received 8 November 2015
Accepted 7 October 2016

KEYWORDS

Change-point detection; dynamic TEM data; hybrid particle growth model; in-situ TEM; normalized particle size distribution; time-varying probability density function

1. Introduction

In situ Transmission Electron Microscopy (TEM) is a promising new technology that is available to scientists seeking to make discoveries in the nanoscale world. In situ TEM uses a special sample holder, allowing motion pictures to be taken as the nano-objects in the sample holder are initiating, crystalizing, and morphing into different sizes and shapes. The unique capability of in situ TEM is that it captures the dynamic changes at the nano or sub-nanoresolution and provides an opportunity to study, and the potential to understand, the mechanisms of multistage growth of nanocrystals. Material scientists point out that understanding and modeling the growth trajectory of nanocrystal are important first steps in the control of the nanocrystal synthesis processes, and expediting discoveries on how a new nanomaterial works (Nehl *et al.*, 2006; Pan *et al.*, 2007). Two in situ TEM video segments of a platinum nanocrystal growth were made available by Zheng *et al.* (2009) as parts of the supplementary material to their publication. The short segment is about 21.2 seconds in duration with 30 frames per second, and the long segment is 76.6 seconds with 15 frames per second. In addition to Zheng *et al.* (2009), a number of other researchers have reported the use of in situ TEM videos in their study of the mechanism of nanocrystal growth (Cheong *et al.*, 2009; Simonsen *et al.*, 2010; Evans *et al.*, 2011; Liu *et al.*, 2013; Woehl *et al.*, 2013).

The current processing technique for in situ TEM videos is largely manual in nature, working typically as follows. Researchers label individual particles in each time frame of the video, measure the sizes of particles, count the number and categorize their shapes, and then plot particle size/shape-related

histograms or report relevant statistics that may lead to some insights into nanocrystal growth. Image processing software is used to facilitate the isolation of overlapped nanocrystals and the measurement of their sizes or aspect ratios (the ratio between long and short axes). One popular tool of this kind is the free-ware ImageJ (ImageJ, 2015), developed by the National Institute of Health, which was used, for instance, in the work of Liu *et al.* (2013). There are also many recent works (Park *et al.*, 2012; Park *et al.*, 2013; Muneesawang *et al.*, 2015) that have significantly improved the accuracy of detecting nanoparticles in TEM images. However, those processing tools can only handle static pictures, one frame at a time, and do not have the ability to extract dynamic information from videos.

Thus, manual processing appears to be a bottleneck preventing scientists from taking full advantage of the capability enabled by the new microscopy technique. Processing video data, considering their sheer volumes and data sizes, is laborious and time-consuming. Processing multiple clips of videos is also repetitive and prone to human error.

More important, one crucial limitation of manual operation is the difficulty in identifying the change points in a nanocrystal growth trajectory going through multiple phases. It is nearly impossible for a person to identify change points accurately by simply looking at the videos; however, nanocrystal growth involving multiple stages is common. Indeed, past experiments have shown that nanocrystal growth can be driven by different kinetics (Zhang *et al.*, 2010; Wang *et al.*, 2013) in various stages. Researchers have developed mathematical models for two kinds of growth mechanisms: the traditional monomer attachment growth, also known as Ostwald ripening (Sholl and

Skodje, 1996; Yang and Zeng, 2004), and non-classic mechanisms, such as orientated attachment (Ribeiro *et al.*, 2005; Xue *et al.*, 2014). To take advantage of these models and describe the dynamics of nanocrystal growth, a data analytic tool is urgently needed for processing the in situ TEM videos and detecting the phase change points to be able to delineate the growth stages.

The lack of an automated tool fulfilling the aforementioned tasks does not come as a surprise, as the nanocrystal growth trajectory is highly stochastic. The current practice, manual in nature, primarily uses some simple size/shape statistics, such as the sample average, to represent the nanocrystal evolution. However, these simple statistics are not sufficient to fully summarize the information in the TEM video data. In recent years, some researchers have made the first step to go beyond simple summary statistics. Park (2014) learned the multiple-path growth trajectory of nano crystals from the in situ or ex situ TEM images. Park *et al.* (2015) proposed a method to track interacting nanocrystals through the growth process in an in situ TEM video. This line of work focuses on tracking an individual nanoparticle growing through various stages. Woehl *et al.* (2013) proposed to identify the growth mechanism based on the Normalized Particle Size Distribution (NPSD). They estimated the NPSD by collecting nanocrystal size information from TEM videos. Since the nanocrystal size measurements from all time frames were pooled together in their work to obtain a single static NPSD, Woehl *et al.* (2013) did not describe the dynamic change underlying the nanocrystal growth.

In this article, we propose a method to estimate the time-varying NPSD—i.e., one NPSD at each time frame—using images from in situ TEM videos. For each time frame, one could fit a probability density function for the normalized nanocrystal sizes, using a standard probability density estimation method, such as the penalized B-spline method (Eilers and Marx, 1996). However, direct application of standard methods does not give good density estimation, due to small sample sizes—there are too few nanocrystals at each time frame. To overcome the small sample size problem, we propose to extend the penalized B-spline density estimation approach in the following way. In the usual penalized B-spline formulation (Eilers and Marx, 1996), the log density function is modeled as a linear combination of B-spline basis functions, and the penalized likelihood method is used to estimate the coefficients of the B-spline expansion. In our extended formulation, the log likelihoods from all time frames are added together and, in addition to the penalty that ensures smoothness of each estimated density function, another penalty term is included to guarantee that the time-varying density functions change smoothly over time. This new formulation of penalized B-splines allows us to borrow information across time frames to obtain a more reliable density estimation.

Under some fixed growth mechanisms, material scientists can use self-similar analytic models to describe the theoretical NPSD (Lifshitz and Slyozov, 1961; Aldous, 1999; Baldan, 2002), which assumes that the NPSD can be approximated by an asymptotic solution at infinite time. Based on that assumption, after the time-varying NPSD is estimated, we can apply a change-point detection method to the estimated density functions to identify the time points of potential phase changes.

In order to facilitate the detection, we discretize each density function into a vector and then apply the Principal Component Analysis (PCA; Jolliffe, 2002) to represent the time-varying NPSD with a small number of Principal Component (PC) scores. After that, state-of-the-art multiple change detection methods, recently developed by Killick *et al.* (2012) and Fryzlewicz (2014), can be used to detect the change points. One problem, however, is that these methods tend to detect more change points than can be explained by our current physical understanding. To address this problem, we propose a selection procedure to choose the significant change points from the candidates identified by an existing methods, using the Sum of Squared Errors (SSE) as the criterion. We stop the selection process when the reduction rate of the SSE is smaller than a threshold. We find that this selection procedure yields a change-point detection result that can be explained by the underlying nanocrystal growth mechanisms. In addition to NPSD, we apply our method to the median particle size to supplement the NPSD-based change-point detection.

With the change points detected using either the NPSD or the median particle size, we are able to partition the particle growth process into several stages, each of which is then described by an existing nanocrystal growth model. We applied this strategy to a published TEM video segment to build a hybrid model for the whole process of nanocrystal growth. Using this new model, we can estimate stage-specific parameters and perform quantitative comparisons of different stages. In a comparison with the single-stage model used by Woehl *et al.* (2013), our hybrid model is shown to be able to describe the nanocrystal growth trajectory more accurately.

The rest of this article is organized as follows. In Section 2, we briefly discuss the need for image preprocessing and then introduce some definitions and notations. In Section 3, we present details on the modeling of the time-varying NPSD. In Section 4, we present our change-point detection approach. In Section 5, we conduct a sensitivity analysis of the tuning parameter used in our detection process. In Section 6, we combine the two mechanistic models, forming a hybrid model for the whole growth stage. Several comparisons are conducted in this section. Finally in Section 7, we conclude our work.

2. Image preprocessing and notations

We describe our methodology using the long segment video provided by Zheng *et al.* (2009) (file name: “1172104s1.mov” in their supplementary material). We select the long segment due to its duration being long enough to contain multiple growth stages. Although using this specific video as an example, the development of our stage identification and change-point detection method is not tailored to this particular example. We believe that our methodology from this section can be readily applied to other in situ TEM videos of nanocrystal growth.

2.1. Video preprocessing

Before identifying the nanocrystal growth, the first step is to detect nanocrystals in the image of each video frame and extract their morphology information. One particular emphasis is to

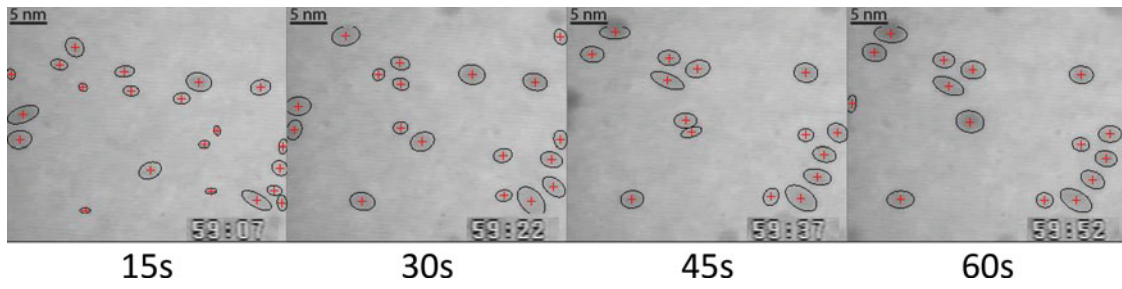


Figure 1. Four frames from the long segment video provided by Zheng *et al.* (2009) and the nanocrystal detection results. The contour line indicates a nanocrystal's edge, whereas the '+' indicates a nanocrystal's center.

address the issue of image segmentation among the aggregated nanoparticles. To fulfill this preprocessing task, we used an image processing method developed by our own team (Qian *et al.*, 2016), which is particularly potent for handling low-contrast and noisy TEM images and outperforms other methods in terms of handling aggregated nanoparticles in similar types of TEM images (Park *et al.*, 2012; Konomi *et al.*, 2013; Park *et al.*, 2013). The detection results at some selected time points are shown in Figure 1.

In this study, as in the original paper (Zheng *et al.*, 2009), we are primarily concerned with the change in nanocrystal size, as the shapes of the nanocrystals are rather uniform. The nanocrystal size is, understandably, characterized by its radius. Denote by r_{st} the radius of the s th particle at time t and by \bar{r}_t the mean radius and \tilde{r}_t the median radius, both at time t . As in Woehl *et al.* (2013) and Zheng *et al.* (2009), the radius r_{st} is defined as $\sqrt{P_{st}/\pi}$, where P_{st} is the area of the corresponding particle.

2.2. Definition of NPSD

Let $G_t(r)$ denote the particle size distribution at time t . The mean radius \bar{r}_t can then be expressed as

$$\bar{r}_t = \int_0^{\infty} r G_t(r) dr. \quad (1)$$

We normalize the nanocrystal size r_{st} at time t by \bar{r}_t to obtain $\phi_{st} = r_{st}/\bar{r}_t$. The normalized particle size distribution, denoted as $F_t(\phi)$, where $\phi = r/\bar{r}_t$, is the distribution of ϕ_{st} at time t . It is easy to see that $F_t(\phi)$ is determined by $G_t(r)$ and \bar{r}_t as

$$F_t(\phi) = \bar{r}_t G_t(\bar{r}_t \phi). \quad (2)$$

Note that both $G_t(\cdot)$ and $F_t(\cdot)$ are time-varying functions, as signified by the subscript t . NPSD provides a better measure of the nanocrystal growth mechanism than the Particle Size Distribution (PSD). Past research (Lifshitz and Slyozov, 1961; Sholl and Skodje, 1996; Woehl *et al.*, 2013) has shown that when the underlying growth mechanism remains the same (within a single stage), the NPSD stays stable, whereas the PSD always changes with the increasing sizes of the nanocrystals. Thus, a change in NPSD can be a strong hint about a new growth mechanism.

3. Penalized B-splines for estimating NPSD

We begin by introducing the estimation of a single probability density function $F_t(\phi)$ from ϕ_{st} at time t using the method of Eilers and Marx (1996). The basic idea is to model the log density

function as a linear combination of B-spline basis functions and then estimate the spline coefficients from the histogram of the observations by maximizing the penalized likelihood. Specifically, the log density can be modeled as

$$\log(F_t(\phi)) = \sum_{j=1}^n a_{jt} B_j(\phi) - C_t, \quad (3)$$

where $B_j(\phi)$ is the j th B-spline basis function, n is the number of basis functions, and

$$C_t = \int_0^{\infty} \sum_{j=1}^n a_{jt} B_j(\phi) d\phi \quad (4)$$

is the normalized constant. Following Eilers and Marx (1996), we create a histogram by dividing the ϕ -axis into m intervals to estimate the spline coefficients (in a B-spline, m is the number of knots). Denote the midpoints as ϕ_i , $i = 1, \dots, m$. Then the B-spline function in Equation (3) evaluated at ϕ_i can be written as

$$\eta_{it} = \sum_{j=1}^n a_{jt} B_j(\phi_i), \quad \forall i = 1, \dots, m. \quad (5)$$

The number of observations falling in the i th interval at the time frame t , denoted by y_{it} , can be assumed to be Poisson distributed with density $\exp(\eta_{it})$. The penalized Poisson likelihood function of $\{a_{jt}\}$ is

$$L_t(\{a_{jt}\}) = \sum_{i=1}^m y_{it} \eta_{it} - \sum_{i=1}^m \exp(\eta_{it}) - \lambda_1 \sum_{j=1}^{n-1} \frac{(\Delta_1 a_{jt})^2}{2}, \quad (6)$$

where Δ_1 is a difference operator with $\Delta_1 a_{jt} = a_{(j+1)t} - a_{jt}$. In the above objective function, the first and second terms correspond to the Poisson likelihood, measuring the goodness-of-fit of $F_t(\phi)$ to the histogram $\{y_{1t}, \dots, y_{mt}\}$; the third term is the roughness penalty, with λ_1 being the penalty parameter, ensuring smoothness of the estimated density. One should maximize $L_t(\{a_{jt}\})$ and then substitute the maximizer $\{\hat{a}_{jt}\}$ to Equation (3) to obtain the estimated probability density $\hat{F}_t(\phi)$ for a single time frame.

When the number of nanocrystals is very small in some time frames, estimating the density functions separately at each time frame does not produce good results. In our revised penalized B-spline formulation, we estimate the density functions by pooling all of the time frame data together. However, unlike Woehl *et al.* (2013), in which the resulting NPSD is a constant function

over the whole growth trajectory, we allow our NPSD to be time-varying, in order to capture the growth dynamics. For this reason, we introduce an additional roughness penalty to ensure that the density functions vary smoothly over time. The new objective function is

$$L(\{a_{jt}\}) = \sum_{t=1}^T L_t(\{a_{jt}\}) - \lambda_2 \sum_{j=1}^n \sum_{t=1}^{T-1} \frac{(\Delta_2 a_{jt})^2}{2}, \quad (7)$$

where Δ_2 is a difference operator with $\Delta_2 a_{jt} = a_{j(t+1)} - a_{jt}$. The λ_2 is the temporal roughness penalty parameter. This new formulation enables information to be borrowed by different time frames, and this improves estimation efficiency, especially at those time frames with an insufficient number of nanocrystals.

We maximize the penalized log likelihood given in Equation (7) to obtain the spline coefficients associated with all of the density functions over the whole growth duration. Apparently, the algorithm developed by Eilers and Marx (1996) is not applicable, as the new formulation has an extra index t and an extra penalty term. The main challenge is caused by the newly introduced second penalty term, which makes the objective function no longer separable with respect to t .

We propose to apply the Alternating Direction Multiplier Method (ADMM) (Boyd *et al.*, 2011) to decouple the the relationships along the t index. Specifically, we replace the a_{jt} in the second penalty term by a set of new variables z_{jt} and solve the optimization problem under the constraints $a_{jt} = z_{jt}$. We perform the constrained optimization by considering the augmented Lagrangian as follows:

$$\begin{aligned} L_\rho(\{a_{jt}\}, \{z_{jt}\}, \{c_{it}\}) &= \sum_{t=1}^T L_t(\{a_{jt}\}) - \lambda_2 \sum_{j=1}^n \sum_{t=1}^{T-1} \frac{(\Delta_2 z_{jt})^2}{2} \\ &\quad - \rho \sum_{t=1}^T \sum_{j=1}^n c_{jt} (a_{jt} - z_{jt}) \\ &\quad - \frac{\rho}{2} \sum_{t=1}^T \sum_{j=1}^n (a_{jt} - z_{jt})^2, \end{aligned} \quad (8)$$

where c_{jt} are the Lagrangian multipliers and ρ is the penalty parameter of the augmented Lagrangian.

Then the ADMM algorithm targets to find the saddle point of Equation (8), defined as

$$(\{\hat{a}_{jt}\}, \{\hat{z}_{jt}\}, \{\hat{c}_{it}\}) = \arg \min_{\{c_{it}\}} \max_{\{a_{jt}\}, \{z_{jt}\}} L_\rho, \quad (9)$$

where $\{\hat{a}_{jt}\}$ is the maximizer of the penalized log likelihood of the density functions. The saddle point is found by using the coordinate descent method (Luenberger, 1973). The idea of the method is as follows. In the q th iteration of updating $\{a_{jt}\}$, $\{z_{jt}\}$, and $\{c_{jt}\}$, first we apply Eilers and Marx's algorithm to find the optimal $\{a_{jt}\}$, given $\{c_{jt}\}$ and $\{z_{jt}\}$ at their current values; then, fixing $\{a_{jt}\}$ and $\{c_{jt}\}$, the Lagrangian is a quadratic form in $\{z_{jt}\}$, whose optimization has a closed-form solution; finally, the Lagrange multipliers $\{c_{jt}\}$ are updated by a "price update" step:

$$c_{jt}^{(q+1)} = c_{jt}^{(q)} + (a_{jt}^{(q)} - z_{jt}^{(q)}). \quad (10)$$

We continue the iteration until all those variables converge. At the convergence of the algorithm, we substitute the convergent values of $\{a_{jt}\}$ to Equation (3) to get the estimated NPSD $\hat{F}_t(\phi)$ for all of the time frames. The detailed steps of the ADMM algorithm are included in the Appendix. We also list the steps of the algorithm in Algorithm 1.

To estimate the NPSD using the video taken by Zheng *et al.* (2009), we set $n = 10$ (the number of B-spline basis), $m = 50$ (the number of knots), and $T = 1148$ (the number of frames in the video). We choose the order of B-spline as two. The estimation is robust with respect to those parameters, so we can choose any reasonable values. The parameter ρ only affects the convergence speed of ADMM, so that as long as the algorithm converges, there is no need to tune it. We set it as 9.0 in this application. The remaining tuning parameters λ_1 and λ_2 can be set by using the Akaike Information Criterion (AIC), as in Eilers and Marx (1996):

$$\text{AIC}(\lambda_1, \lambda_2) = \text{dev}(\lambda_1, \lambda_2) + 2\text{dim}(\lambda_1, \lambda_2), \quad (11)$$

where $\text{dev}(\lambda_1, \lambda_2)$ is the deviance of the estimated curves, and $\text{dim}(\lambda_1, \lambda_2)$ is the effective dimension of parameters. The deviance is defined as

$$\text{dev}(\lambda_1, \lambda_2) = 2 \sum_{t=1}^T \sum_{i=1}^m y_{it} \ln y_{it} - 2 \sum_{t=1}^T \sum_{j=1}^n \hat{a}_{jt} B_{jt}^+. \quad (12)$$

And we define the effective dimension of parameters as

$$\text{dim}(\lambda_1, \lambda_2) = \text{tr}\{(B'B + \lambda_1 D_1' D_1)^{-1} B'B\} \text{tr}\{(I_T + \lambda_2 D_2 D_2')^{-1}\}, \quad (13)$$

where $\text{tr}\{\cdot\}$ is the trace of the corresponding matrix. By minimizing $\text{AIC}(\lambda_1, \lambda_2)$, the two tuning parameters are chosen as $\lambda_1 = 0.5$, $\lambda_2 = 1.5$.

Algorithm 1 Procedure for solving the revised penalized B-spline density estimation

1. Set tuning parameters m , n , λ_1 , λ_2 , and ρ .
2. Construct the B-spline basis function $B_j(\phi_i)$ according to the knots ϕ_i for $i = 1, \dots, m$ and $j = 1, \dots, n$. Then we calculate $B_t^+ = [B_{1t}^+, \dots, B_{mt}^+]$ and $B_{jt}^+ = \sum_s B_j(\phi_{st})$.
3. Initialize $A^{(0)}$, $Z^{(0)}$, and $C^{(0)}$. We recommend setting $(H^{(0)})_{it} = \log(y_{it})$, $A^{(0)} = Z^{(0)} = B^{-1}H^{(0)}$, and $C^{(0)} = \mathbf{0}$.
4. Set $q = 0$.
5. Update $A^{(q+1)}$. For $t = 1, \dots, T$, we update each column of $A^{(q+1)}$ as follows:
 - (a) Set $\hat{a}_t = a_t^{(q)}$.
 - (b) Solve the following equation:

$$\begin{aligned} B_t^+ - B' \exp(B\hat{a}_t) + B'B\hat{a}_t + \rho (z_t^{(q)} - c_t^{(q)}) \\ = [B'B + \lambda_1 D_1' D_1 + \rho I_n] a_t, \end{aligned} \quad (14)$$

where \hat{a}_t is the estimate from the previous iteration, and D_1 is an $n \times n$ matrix with $(D_1)_{jj}$ as -1 , $(D_1)_{j(j-1)}$ as 1, for $j = 2, \dots, n$, and all other elements as 0. Use the solution of a_t to update \hat{a}_t .

- (c) Repeat the previous step until \hat{a}_t converges, then let $a_t^{(q+1)} = \hat{a}_t$.

6. Update $Z^{(q+1)}$ by solving the following equation:

$$Z^{(q+1)} = [A^{(q+1)} + C^{(q)}] \left(I_T + \frac{\lambda_2}{\rho} D_2 D_2' \right)^{(-1)}, \quad (15)$$

where D_2 is a $T \times T$ matrix with $(D_2)_{tt}$ as -1 , $(D_2)_{t(t+1)}$ as 1, for $t = 1, \dots, T - 1$, and all other elements as 0.

7. Update $C^{(q+1)}$ via the following equation:

$$C^{(q+1)} = C^{(q)} + (A^{(q+1)} - Z^{(q+1)}), \quad (16)$$

then let $q = q + 1$.

8. Repeat Step 5 to 7 until A , Z , and C all converge.

We show in Figure 2 the NPSDs estimated at $t = 10, 40$, and 70 seconds. The same approach can also be used to estimate PSD, by replacing the observations ϕ_{st} with r_{st} and replacing knots ϕ_i with r_i . The parameters $m, n, T, \lambda_1, \lambda_2$, and ρ are set the same as those used in the estimation of NPSD. The PSDs estimated at $t = 10, 40$, and 70 seconds are shown in Figure 3.

4. Change-point detection

The estimated NPSD $\hat{F}_t(\phi)$ is available to us as a vector at each t ; i.e., $\{\hat{F}_t(\phi_1), \dots, \hat{F}_t(\phi_m)\}$. To detect a change point in $\hat{F}_t(\phi)$ amounts to a multivariate detection problem, and a common strategy to make such a detection procedure effective is to reduce the dimension of the vector by using PCA (Jolliffe, 2002). PCA attempts to find a small number of significant projections of the original vector onto a lower-dimensional space, which is supposed to closely represent the original vector. When applying PCA to our NPSD, it turns out that only the first PC is significant. In Figure 4, we plot the first 10 eigenvalues corresponding

to the respective PCs, as well as the scores of the first and second PCs. The eigenvalue of the first PC is much larger than that of the other PCs. In fact, the first PC explains 86.5% of the total variance of the original data. In addition to considering the numerical percentage of the first PC, we observe that its score exhibits a clear pattern, whereas that of the second PC appears random, underpinning the decision to use only the first PC for our detection purpose. Thus, in the following, we work with the scores of the first PC, which is denoted by \hat{p}_t . However, we want to note that it is not always the case that only the first PC is significant. In the case where there is more than one significant PC, we would apply a multivariate change-point detection framework, such as the methods of Zamba and Hawkins (2006), on the scores of the significant PCs.

Without knowing the exact number of possible change points in the process, a popular treatment, known as the Binary Segmentation Process (Yao, 1988, BSP), can be used to detect the most significant change point first and then continue applying the same detection method to the subsequences before and after the detected change point. The dominating criterion used in the existing BSP methods to decide the existence of a change point is the Bayesian Information Criterion (BIC; Schwarz (1978)). However, if we apply the BSP method with BIC as the stopping criterion to our data, it finds more than 400 change points, obviously over-segmenting the nanocrystal growth trajectory. We also tried some state-of-the-art multiple change-point detection methods, such as the Pruned Exact Linear Time (PELT; Killick *et al.* (2012)) and the Wild Binary Segmentation (WBS; Fryzlewicz (2014)), but they also returned more change points than what the mechanisms can explain (eight change points when using PELT and 49 when using WBS).

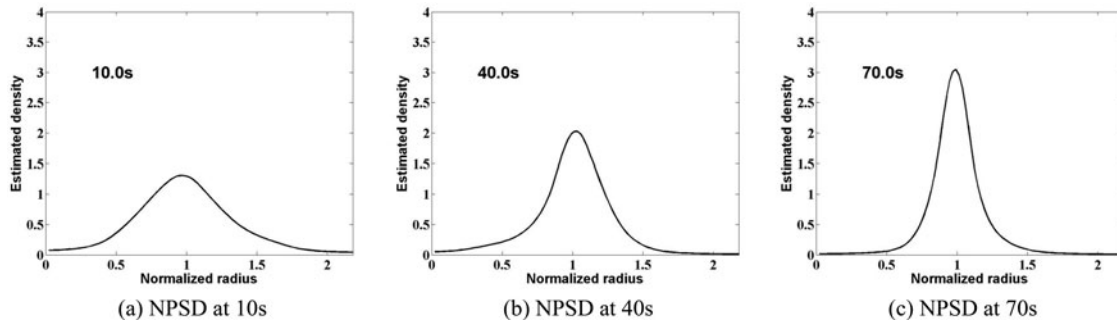


Figure 2. The estimated NPSDs at 10, 40, and 70 seconds.

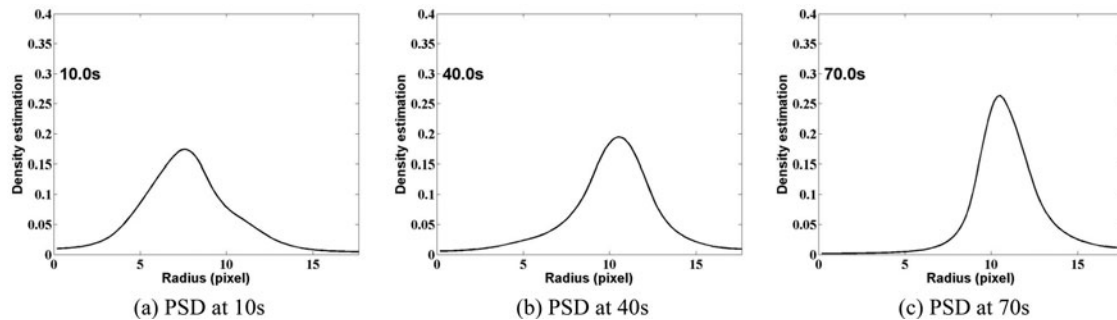


Figure 3. The estimated PSDs at 10, 40, and 70 seconds.

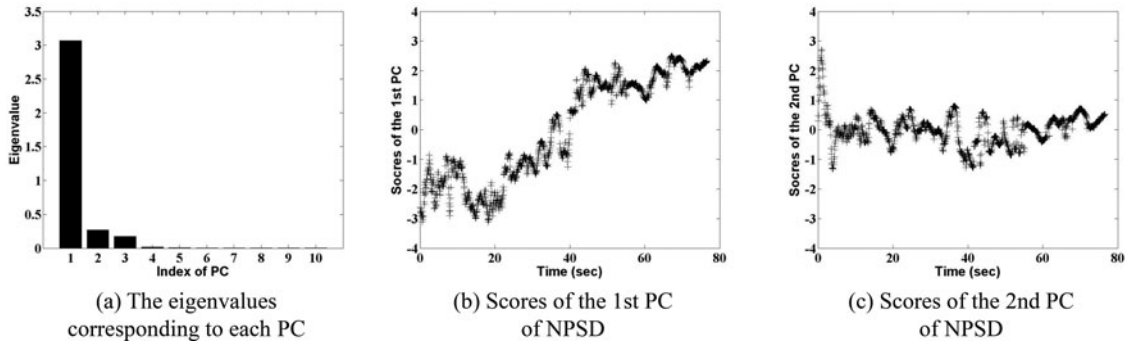


Figure 4. PCA of the NPSD: (a) the eigenvalues corresponding to the first 10 PCs; (b) the scores of the first PC; and (c) the scores of the second PC.

Apparently, we need to reduce the number of change points to be consistent with physical understanding. In doing so, we found that a robust criterion to select the change points is the reduction rate in the SSE of the piecewise constant model before and after a change point is added. Recall that NPSD is supposed to stay stable within each growth stage so that the scores of the NPSD's PCs should fluctuate around a constant within a growth stage. If all of the change points are correctly identified, the piecewise constant model for fitting the scores of the NPSD's PC should produce the lowest SSE.

Given all of the candidate change points detected by one of the popular methods (we chose PELT here, as it returned the fewest change points among all methods we explored), we start with a constant model and then test each of those candidates. We pick the first potential change point to be the place where the largest reduction of SSE can be achieved by the two piecewise constant models. If the reduction in SSE is large enough, we believe this change point to be genuine and continue the selection process. Then, we visit all of the remaining candidates to find the next change point that gives the largest reduction rate in SSE. We repeat the same step until the reduction of SSE is no longer significant, suggesting that the difference between the two piecewise constant models is most likely due to random noise rather than to a substantial change in the process. The detailed steps are described as follows.

Suppose we have already found $c - 1$ change points, denoted as $\hat{t}_1, \dots, \hat{t}_{c-1}$, while there are g remaining candidates, denoted as $\tilde{t}_1, \dots, \tilde{t}_g$. The next possible change point chosen from $\tilde{t}_1, \dots, \tilde{t}_g$ is denoted as t_c . They together segment the whole data sequence into $c + 1$ subsequent events, denoted by $S_e, e = \{1, \dots, c + 1\}$. The overall SSE of the piecewise constant model

fitting of \hat{p}_t is computed as

$$V(\hat{t}_1, \dots, \hat{t}_{c-1}, t_c) = \sum_{e=1}^{c+1} \sum_{t \in S_e} (\hat{p}_t - b_0^{(e)})^2, \quad (17)$$

where $b_0^{(e)}$ is the mean of \hat{p}_t within S_e . The position of the next potential change point is determined by

$$\hat{t}_c = \arg \min_{t_c \in (\tilde{t}_1, \dots, \tilde{t}_g)} V(\hat{t}_1, \dots, \hat{t}_{c-1}, t_c). \quad (18)$$

Then we delete \hat{t}_c from the candidates $\{\tilde{t}_1, \dots, \tilde{t}_g\}$ and continue the selection process, until there is no remaining change-point candidate.

By applying Equation (17) to the in situ TEM data of our example, we found a series of potential change points from the eight candidates detected by PELT, which are shown in Figure 5(a). Figure 5(b) presents the profile of the SSE, $V(\hat{t}_1, \dots, \hat{t}_c)$, in which $\hat{t}_{(1)}, \dots, \hat{t}_{(8)}$ represents the order of the selection. We deem a potential change point \hat{t}_c a genuine change point if the reduction rate of the SSE is larger than a threshold θ :

$$\frac{V(\hat{t}_1, \dots, \hat{t}_{c-1}) - V(\hat{t}_1, \dots, \hat{t}_c)}{V(\hat{t}_1, \dots, \hat{t}_{c-1})} > \theta. \quad (19)$$

In other words, if including \hat{t}_c reduces the SSE by more than $\theta \times 100\%$, we tend to believe that the change point is due to a true process change rather than random noise. Then we continue the selection for the next potential change point. If the criterion in Equation (19) is not satisfied, we consider that all of the significant change points have been found and stop the process.

We want to note that the PC scores are autocorrelated, a result of the temporal penalty added in our density estimation step.

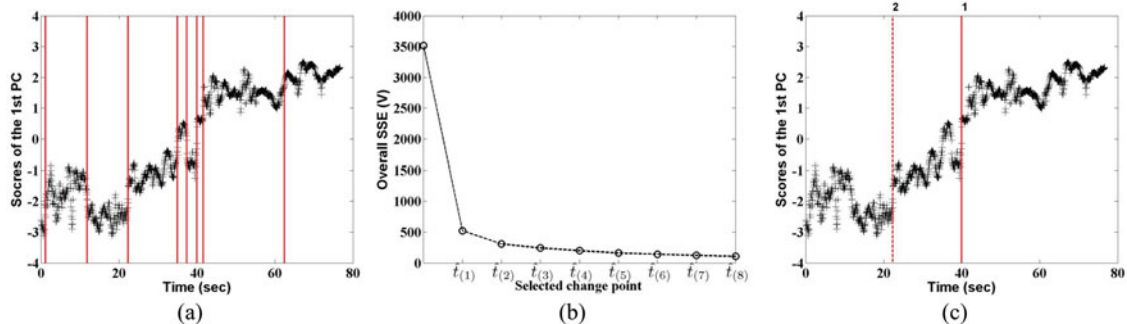


Figure 5. Results of the proposed change-point detection using size distribution: (a) eight potential change-point candidates detected by PELT; (b) change in $V(\cdot)$ when selecting a change point at a time; and (c) all change points detected when θ is varied in the range of (0.2, 0.8).

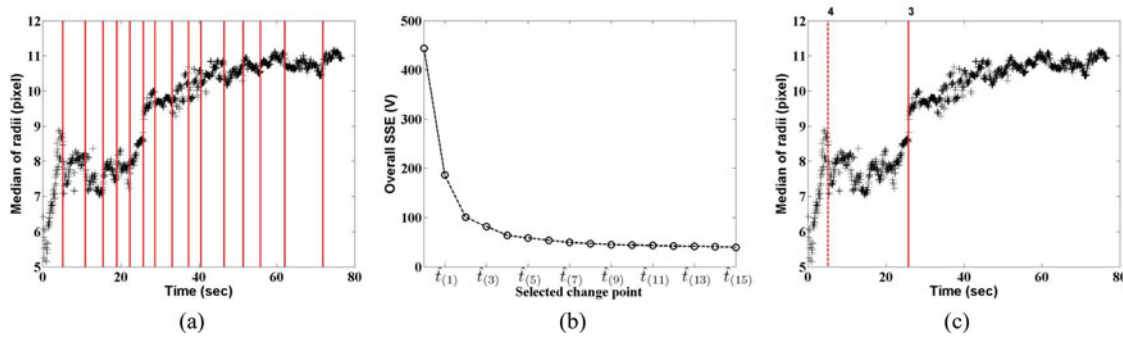


Figure 6. Results of the proposed change-point detection using median particle size: (a) 15 potential change points detected by `strucchange` package; (b) change in $V(\cdot)$ when selecting a change-point at a time; and (c) all change points detected when θ is varied in the range of (0.2, 0.8).

If the PC score is severe and causing too many false alarms, the autocorrelation in the PC scores may need to be removed before a change-point detection method is applied. We recommend using a model-free approach such as the unweighted batch mean (Runger *et al.*, 1995).

The same strategy can also be applied to a simple statistic, such as the median or mean particle size, which has often been used to describe nanocrystal growth, due to its simplicity. As the median radius is less sensitive to outliers, we apply our method to the median particle size \tilde{r}_t , instead of the mean particle size \bar{r}_t . Unlike the NPSD, which remains relatively stable without a change point, so that its PC fluctuates around a constant, \tilde{r}_t exhibits an increasing trend along the growth process.

What we needed to do was to revise the detection process to handle the trend. We adopted the `strucchange` package (Kleiber *et al.*, 2002), which detects change points after a regression, and using it we found 15 change-point candidates. To select the significant change points, we first applied a detrending operation before performing the change-point detection. Following Chen and Gupta (2001), we used a linear model to de-trend the median particle size. Hence, we revised the SSE by using the residuals after fitting a piecewise linear trend model, as follows:

$$V(\hat{t}_1, \dots, \hat{t}_{c-1}, t_c) = \sum_{e=1}^{c+1} \sum_{t \in S_e} (\tilde{r}_t - b_0^{(e)} - b_1^{(e)}t)^2, \quad (20)$$

where $b_0^{(\cdot)}$ and $b_1^{(\cdot)}$ are the coefficients of the respective linear model. After the definition of SSE was revised, the rest of the procedure for NPSD was adapted to select the significant change points in \tilde{r}_t . Figure 6(a) and 6(b) present the intermediate detection results in our example while using the median size.

The key tuning parameter in this selection procedure is θ . In our application, we set $\theta = 0.5$ for both NPSD and the median particle size. The choice of $\theta = 0.5$ means that we deem a candidate a genuine change point if its selection reduces the SSE by half or more. By this choice, we detected one change point in NPSD and another one in median size; the two change points are shown as “#1” in Figure 5(c) and “#3” in Figure 6(c), respectively. For future applications, we would recommend the same choice for θ .

Setting $\theta = 0.5$, the change-point detection method produces two phase change points: at 25.8 seconds in \tilde{r}_t (“#3” in Figure 6(c)) and at 39.9 seconds in NPSD (“#1” in Figure 5(c)).

These two change points segment the whole growth trajectory into three stages: (0, 25.8), (25.8, 39.9), and (39.9, 76.6) seconds. The delineated stages make it immediately clear how the nanocrystals grow: they go through two major growth stages with a transition stage in between. For this particular process, the two dominating mechanisms have been studied and understood (Zheng *et al.*, 2009; Zhang *et al.*, 2010; Bian *et al.*, 2013; Wang *et al.*, 2013): in the period of (0, 25.8) seconds, the Orientated Attachment (OA) mechanism dominates, whereas in the period of (39.9, 76.6) seconds, the Ostwald Ripening (OR) mechanism dominates. It is understandable that the mechanism change does not happen suddenly. As one mechanism gradually takes over from the other, a short transition period naturally exists, which is the period of (25.8, 39.9) seconds in this example.

5. Sensitivity of tuning parameter θ

Given the critical role played by θ , we conducted a sensitivity analysis. Figure 7 shows the number of change points detected in both the NPSD and median size methods, as θ varies in the range of (0.2, 0.8). The NPSD-based detection produces either one change point or two change points. The first change point detected in the two-point case is the same as the change point detected in the single-point case, shown as

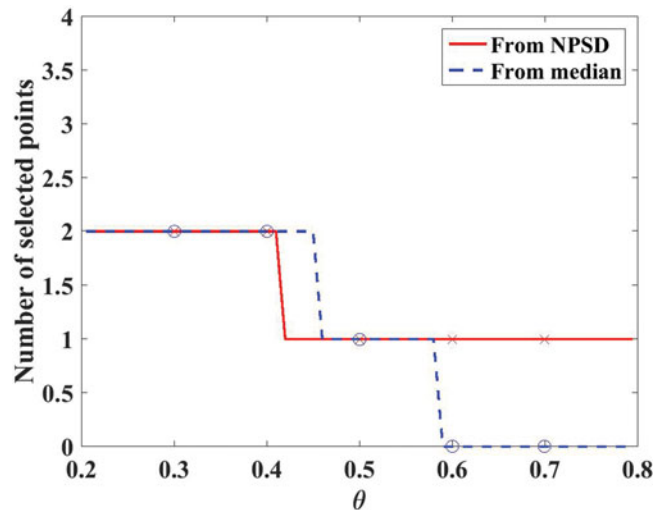


Figure 7. The number of change points detected in NPSD and median particle size approach for $\theta \in (0.2, 0.8)$.

“#1” in Figure 5(c). The second change point is shown as “#2” in the same figure. The median-size-based detection method is more sensitive to the value of θ : it produces between zero and two change points over the same θ range. The two change points that could have been detected are marked as “#3” and “#4”, respectively, in Figure 6(c). In addition to the sensitivity issue, another drawback of using the median size statistic is that one would not be able to detect “#1” unless setting θ to some extreme value (like 0.1); given the analysis done by Zheng *et al.* (2009), we know that a phase change indeed occurred around the time of “#1,” so that missing this change point is a serious limitation.

When looking closely at the four possible change points, it is apparent to us that the change points “#2” and “#3” are the outcome of the same change, as their time stamps are only 3.2 seconds apart. By merging “#2” and “#3,” the change-point detection outcomes could possibly segment the whole growth into four stages, three stages, or two stages, depending the specific choice of θ . However, an important message, we believe, is that the difference in the detection outcome does not lead to a drastically different understanding of the basic science underpinning the process. To see this point, consider the following alternatives.

When a smaller θ is used, all four change points could have been detected. Having “#4” apparently suggests the existence of an initial nucleation stage, which is generally hard to observe, as its duration is short, data variability is high, and the number of nanocrystals is small. Missing this initial stage is understandable and not seriously detrimental to the subsequent analysis.

Had we chosen a large θ (say, greater than 0.6), only one change point (#1 in Figure 5(c)) would be detected in NPSD and no change point in the median size approach. Hence, the transition stage could have been missed. Still, we would not miss the big picture of two dominating growths; i.e., OA and OR.

The overall analysis shows that the NPSD-based detection outcome is robust, as it captures the important change points consistently in a broad range of the tuning parameter. To avoid missing potentially important change points in future applications, one should vary θ in a reasonable range and then choose a manageable number of the change points.

The fact that NPSD-based detection produces a rather robust detection that separates the whole growth trajectory into two major stages speaks to the benefit of having such a detection approach. Had we not known the individual mechanisms under respective stages, this detection outcome would hint strongly at

where to explore to obtain an understanding of the basic science driving the growth process.

6. Hybrid modeling

In this application, since we do know the dominating growth mechanisms, we can adopt the existing first-principle models for each respective growth stage and then use an interpolation to model the transition period. As such, we produce a unified growth model, as a hybrid of the first principle based model and the empirical model, for the whole nanocrystal growth trajectory.

The models for NPSD $\hat{F}_t(\phi)$ and mean particle size \bar{r}_t during the OA growth in the first stage (0, 25.8) seconds, taken from the work of Aldous (1999), are, respectively:

$$F_{t_{OA}}(\phi) = \frac{2W_{OA}}{\Gamma(a_{OA} + 1)} (W_{OA}\phi)^{2a_{OA}+1} e^{-(W_{OA}\phi)^2},$$

$$\bar{r}_{t_{OA}}^{2(a_{OA}+1)} = b_{OA}(t - t_{OA}), \quad (21)$$

where $W_{OA} = (a_{OA} + 1)\Gamma(a_{OA} + 3/2)/\Gamma(a_{OA} + 1)$. The three parameters used in the two models are a_{OA} , indicating the variance of the process, b_{OA} , indicating the growth rate, and t_{OA} , indicating the initial size of nanocrystals.

The kinetics of OR growth in the third stage (39.9, 76.6) seconds is usually described by the LSW model (Lifshitz and Slyozov, 1961). Thus, we also chose to use the LSW model to represent the mean particle size (\bar{r}_t) growth in the OR stage. For the \bar{r}_t growth, the LSW approach models the cube of \bar{r}_t with a linear function. The model of \bar{r}_t growth in the OR stage bears a similar appearance to the model of \bar{r}_t in the OA stage but the key difference is the different power term on \bar{r}_t .

However, to model $\hat{F}_t(\phi)$ in the OR growth part, we found that the LSW model cannot obtain a good fit for the estimated $\hat{F}_t(\phi)$. In Figure 8, we compare the empirical NPSDs estimated at 45 and 70 seconds with the NPSD derived from the LSW model. The two empirical NPSDs are similar, and both of them look rather symmetric. The LSW-based NPSD is more skewed with a long lower tail and has larger variance compared with the empirical NPSDs. The long lower tail of the LSW-based NPSD presents a clear contrast with the NPSDs estimated directly from the data. In our opinion, there are two reasons for the mismatch. First, the smaller particles are difficult to track under the current resolution of the in situ TEM, yet the LSW model, with a long

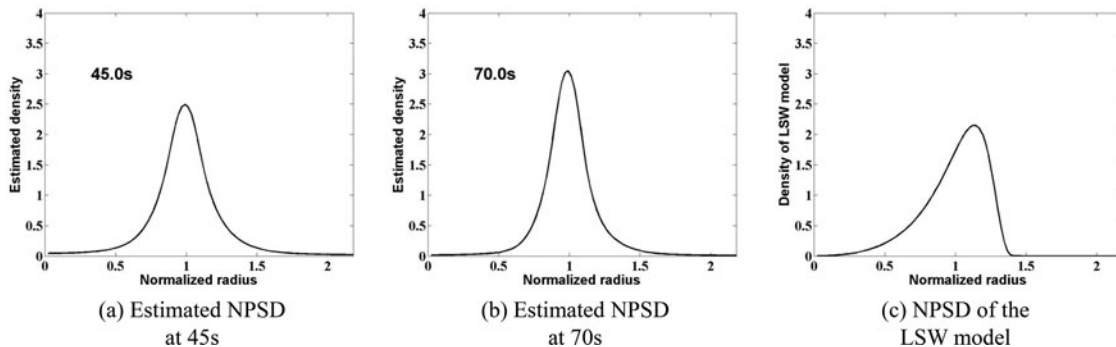


Figure 8. (a) The empirical NPSD estimated at 45 seconds; (b) the empirical NPSD estimated at 70 seconds; and (c) the theoretical NPSD derived from the LSW model.

Table 1. The estimated parameters associated with the two stages in the nanocrystal growth.

a_{OA}	b_{OA}	t_{OA}	a_{OR}	b_{OR}	t_{OR}
1.47	42.2	-429.3	7.31	0.55	-1342.7

left tail, is more sensitive to the missed detection of these particles. Second, the LSW model is known to be inconsistent in its interpretation of experimental results (Voorhees, 1985). For this reason, researchers have proposed modified models to improve the fitting accuracy (Hardy and Voorhees, 1988; Lo and Skodje, 2000; Baldan, 2002), but when these models were tested against the TEM video data at hand, they did not produce a higher fitting quality. Thus, we decided to use the OA growth model structure (derived by the Smoluchowski equation) to fit for NPSD in the OR growth; doing so indeed produced a better fit. The added benefit of using the same model structure in both stages is that it makes their comparison easier. Specifically, the OR growth models are

$$F_{t_{OR}}(\phi) = \frac{2W_{OR}}{\Gamma(a_{OR} + 1)} (W_{OR}\phi)^{2a_{OR}+1} e^{-(W_{OR}\phi)^2},$$

$$\bar{r}_{t_{OR}}^3 = b_{OR}(t - t_{OR}). \quad (22)$$

The first equation here is the same as that in Equation (21) but with different parameters. The three parameters used in the OR models share the same interpretations as those in the OA model.

Using the TEM data, we estimated the parameters associated with the two stages, presented in Table 1. Compared with a_{OA} , the larger a_{OR} suggests that a larger variance of NPSD in the OR growth. This conclusion is consistent with the observations made by Zheng *et al.* (2009), but our result provides a quantitative contrast. Using the estimated values of b_{OA} and b_{OR} , we calculated the derivative of \bar{r}_t for the two stages. For the OA growth, the derivative was calculated as

$$\frac{d\bar{r}_t}{dt} = \frac{1}{2(a_{OA} + 1)} b_{OA} [b_{OA}(t - t_{OA})]^{-\frac{1}{2(a_{OA}+1)} - 1}, \quad (23)$$

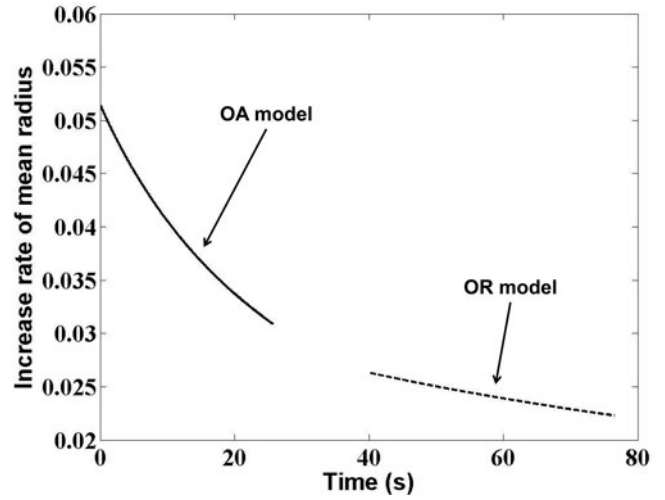
and for the OR growth, the derivative is calculated as

$$\frac{d\bar{r}_t}{dt} = \frac{1}{3} b_{OR} [b_{OR}(t - t_{OR})]^{-\frac{1}{3} - 1}. \quad (24)$$

In Fig. 9, we compare the derivatives for the OA and OR growth. The gap between the two curves corresponds to the transition period, for which no theoretical model is yet available. The two curves make it clear that in the nanocrystal growth, the mean radius growth rate in the OA stage is faster than that in the OR stage, just as the estimated b_{OA} and b_{OR} values suggested. This was again stated by Zheng *et al.* (2009), but our analysis provides a quantitative picture of the mean radius evolution in the two stages.

The difference in t_{OA} and t_{OR} suggests that the initial nanocrystal sizes are different, and a more negative quantity implies a large initial size. The t_{OA} and t_{OR} values in Table 1 make perfect sense, as the OR growth follows the OA growth, so that the initial nanocrystals in OR have a bigger size.

To include the transition period between (25.8, 39.9) seconds, we introduced the weighting functions $\lambda_N(t)$ and $\lambda_R(t)$ for NPSD and mean particle size, respectively, to combine the two aforementioned models. The two weighting functions have

**Figure 9.** The comparison of the first derivative of \bar{r}_t in the OA and OR growth stages.

a value of zero when $t < 25.8$ seconds, one when $t > 39.9$ seconds, and increase from zero to one quadratically in between, with their quadratic function coefficients fitted from the corresponding NPSD or mean particle size in the transition period. The overall growth models of $F_t(\phi)$ and \bar{r}_t , respectively, in this hybrid structure can be written as

$$F_t(\phi) = (1 - \lambda_N(t))F_{t_{OA}}(\phi) + \lambda_N(t)F_{t_{OR}}(\phi),$$

$$\bar{r}_t = (1 - \lambda_R(t))\bar{r}_{t_{OA}} + \lambda_R(t)\bar{r}_{t_{OR}}. \quad (25)$$

To verify the quality of our hybrid growth model, we show in Figure 10(a) the SSE values between the $F_t(\phi)$ simulated using Equation (25) and its empirically estimated counterpart directly using the TEM observations. Except for the beginning few seconds and the transition period, the simulated results closely follow the empirical results. The relatively worse fit during the transition period is understandable, as there is a lack of theories to describe the transition mechanism. We also fitted Woehl *et al.*'s (2013) single-stage model and show its SSE in Figure 10(a). Our hybrid model produces smaller SSE values for both the OA and OR growth stages and it is comparable to Woehl *et al.*'s model in the transition period.

The above learning results provide a quantitative model to describe the whole growth trajectory. Using the learned results, we can simulate the evolution of PSD, $G_t(r)$, using the hybrid model of \bar{r}_t and $F_t(\phi)$, as

$$G_t(r) = \frac{1}{\bar{r}_t} F_t\left(\frac{r}{\bar{r}_t}\right). \quad (26)$$

We estimated the PSD based directly on the observations of r_{st} by using the proposed non-parametric density estimation method. The SSE curve between the simulated PSD and the estimated PSD is shown in Fig. 10(b). Additionally, we show the SSE curves between the estimated PSD and the PSDs simulated by using, respectively, Woehl *et al.*'s (2013) single-stage model, the OA growth model alone, and the OR growth model alone. The hybrid growth model fits the observed data consistently well throughout the entire growth trajectory, whereas the other models all have deficiencies in certain periods.

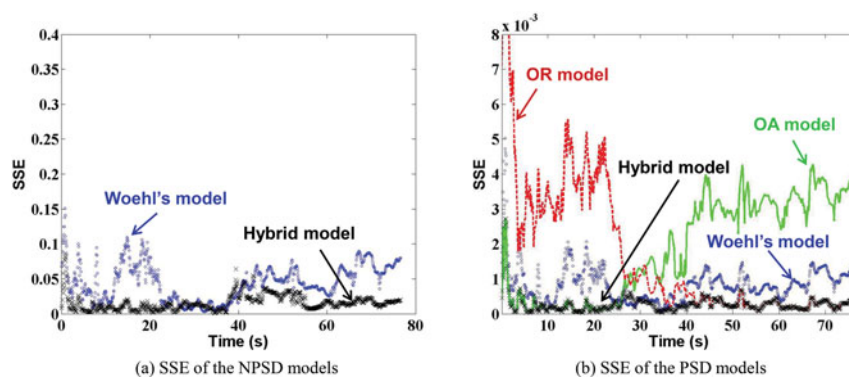


Figure 10. A comparison of the simulated results and the empirical estimation from the data: (a) the SSE curves between the simulated NPSD (by using the hybrid model or Woehl's model) and its estimated counterpart; and (b) the SSE curves between the simulated PSDs (by using the hybrid model, Woehl's model, OA model alone, and OR model alone, respectively) and their estimated counterpart.

7. Concluding remarks

In this article, we proposed a method aimed at identifying and delineating different stages in nanocrystal growth using in situ TEM videos, assuming that a self-similar analytic solution existed for a fixed growth mechanism. We make two major contributions: the first is to estimate a time-varying NPSD by pooling data from all time frames and develop a modified penalized B-spline method accordingly; the second is to perform a robust change-point detection of the highly stochastic nanocrystal growth process, providing a detection outcome consistent with physical understanding. We applied our change-point analysis to a published in situ TEM video clip.

Our work shows the importance of using probability distribution functions, not the simple statistics, for phase identification and model-building purposes. It also reveals the existence of a transition period between the two main growth stages. The existence of the transition period is expected, and our method finds its precise timing. However, the underlying mechanism of the transition period is still poorly understood. Our hybrid model, which assumes a linear combination of the two main growth mechanisms in the transition period, provides an initial attempt to solve the problem and fits the observations reasonably well. Moreover, the estimated time-varying NPSD gives additional evidence that the LSW model does not fit experiment results well at the latter stage. We hope that our method can help material scientists find an accurate theoretical model for predicting the long-time distribution of OR. Overall, we believe that our detection and modeling efforts lay a foundation for future quality control of nanocrystal synthesis processes. With the density estimation and the predictive model, engineers can monitor the process and detect the out-of-control situations by comparing the observed and theoretical distributions.

Funding

This work is partially supported by NSF grant CMMI-1000088 (to YJQ and YD), by AFOSR DDDAS program grant FA9550-13-1-0075 (to YJQ, JZH, and YD), and NSF grant DMS-1208952 (to JZH).

Notes on contributors

Yanjun Qian received a B.S. (2009) and M.S. (2012) in Automation from Tsinghua University, China. He is currently a Ph.D. candidate in Industrial & Systems Engineering at Texas A&M University. His research interests are in system informatics and quality and reliability engineering, image

and video processing, and machine learning. He is a student member of INFORMS.

Jianhua Z. Huang received a B.S. in Probability and Statistics from Beijing University of China (1989); an M.S. in Probability and Statistics from Beijing University of China (1992); and a Ph.D. in Statistics from University of California at Berkeley (1997). He is currently a Professor of Statistics at Texas A&M University. His research interests are in statistical machine learning and applied statistics. He is a fellow of ASA and IMS and an elected member of ISI.

Yu Ding received a B.S. in Precision Engineering from the University of Science & Technology of China (1993); an M.S. in Precision Instruments from Tsinghua University, China (1996); an M.S. in Mechanical Engineering from Penn State University (1998); and a Ph.D. in Mechanical Engineering from the University of Michigan (2001). He is currently the Mike and Sugar Barnes Professor of Industrial & Systems Engineering and Professor of Electrical & Computer Engineering at Texas A&M University. His research interests are in system informatics and quality and reliability engineering. He is a fellow of IISE, a fellow of ASME, a senior member of IEEE, and a member of INFORMS.

References

- Aldous, D. (1999) Deterministic and stochastic models for coalescence (aggregation and coagulation): A review of the mean-field theory for probabilists. *Bernoulli*, **5**, 3–48.
- Baldan, A. (2002) Review progress in Ostwald ripening theories and their applications to nickel-base super alloys, Part I: Ostwald ripening theories. *Journal of Materials Science*, **37**(11), 2171–2202.
- Bian, B., Xia, W., Du, J., Zhang, J., Liu, J. P., Guo, Z. and Yan, A. (2013) Growth mechanisms and size control of FEPT nanoparticles synthesized using $\text{Fe}(\text{Co})_x (x < 5)$ -oleylamine and platinum(II) acetylacetonate. *Nanoscale*, **5**(6), 2454–2459.
- Boyd, S., Parikh, N., Chu, E., Peleato, B. and Eckstein, J. (2011) Distributed optimization and statistical learning via the alternating direction method of multipliers. *Foundations and Trends in Machine Learning*, **3**(1), 1–122.
- Chen, J. and Gupta, A.K. (2001) On change point detection and estimation. *Communications in Statistics - Simulation and Computation*, **30**(3), 665–697.
- Cheong, S., Watt, J., Ingham, B., Toney, M. and Tilley, R. (2009) In situ and ex situ studies of platinum nanocrystals: growth and evolution in solution. *Journal of the American Chemical Society*, **131**(40), 14590–14595.
- Eilers, P. and Marx, B. (1996) Flexible smoothing with B-splines and penalties. *Statistical Science*, **11**(2), 89–102.
- Evans, J.E., Jungjohann, K.L., Browning, N.D. and Arslan, I. (2011) Controlled growth of nanoparticles from solution with in situ liquid transmission electron microscopy. *Nano Letters*, **11**(7), 2809–2813.
- Fryzlewicz, P. (2014) Wild binary segmentation for multiple change-point detection. *The Annals of Statistics*, **42**(6), 2243–2281.

- Hardy, S. and Voorhees, P. (1988) Ostwald ripening in a system with a high volume fraction of coarsening phase. *Metallurgical Transactions A*, **19**(11), 2713–2721.
- ImageJ. (2015) Image processing and analysis in Java, version 1.50d. Available at <http://rsbweb.nih.gov/ij/>. [29 December 2016].
- Jolliffe, I.T. (2002) *Principal Component Analysis*, Springer-Verlag, New York, NY.
- Killick, R., Fearnhead, P. and Eckley, I. (2012) Optimal detection of change-points with a linear computational cost. *Journal of the American Statistical Association*, **107**(500), 1590–1598.
- Kleiber, C., Hornik, K., Leisch, F. and Zeileis, A. (2002) strucchange: An R package for testing for structural change in linear regression models. *Journal of Statistical Software*, **7**(2), 1–38.
- Konomi, B., Dahvala, S.S., Huang, J.Z., Kundu, S., Huitink, D., Liang, H., Ding, Y. and Mallick, B.K. (2013) Bayesian object classification of gold nanoparticles. *The Annals of Applied Statistics*, **7**(2), 640–668.
- Lifshitz, I. and Slyozov, V. (1961) The kinetics of precipitation from supersaturated solid solutions. *Journal of Physics and Chemistry of Solids*, **19**(1), 35–50.
- Liu, Y., Tai, K. and Dillon, S.J. (2013) Growth kinetics and morphological evolution of ZnO precipitated from solution. *Chemistry of Materials*, **25**(15), 2927–2933.
- Lo, A. and Skodje, R.T. (2000) Kinetic and Monte Carlo models of thin film coarsening: Cross over from diffusion-coalescence to Ostwald growth modes. *The Journal of Chemical Physics*, **112**(4), 1966–1974.
- Luenberger, D.G. (1973) *Introduction to Linear and Nonlinear Programming*, Addison-Wesley, Boston, MA.
- Muneesawang, P., Sirisathitkul, C. and Sirisathitkul, Y. (2015) Multi-level segmentation procedure for measuring the size distribution of nanoparticles in transmission electron microscope images. *Science of Advanced Materials*, **7**(4), 769–783.
- Nehl, C., Liao, H. and Hafner, J. (2006) Optical properties of star-shaped gold nanoparticles. *Nano Letters*, **6**(4), 683–688.
- Pan, Y., Neuss, S., Leifert, A., Fischler, M., Wen, F., Simon, U., Schmid, G., Brandau, W. and Jahn-Dechent, W. (2007) Size-dependent cytotoxicity of gold nanoparticles. *Small*, **3**(11), 1941–1949.
- Park, C. (2014) Estimating multiple pathways of object growth using non-longitudinal image data. *Technometrics*, **56**(2), 186–199.
- Park, C., Huang, J.Z., Huitink, D., Kundu, S., Mallick, B.K., Liang, H. and Ding, Y. (2012) A multistage, semi-automated procedure for analyzing the morphology of nanoparticles. *IEE Transactions*, **44**(7), 507–522.
- Park, C., Huang, J.Z., Ji, J.X. and Ding, Y. (2013) Segmentation, inference and classification of partially overlapping nanoparticles. *IEEE Transactions on Pattern Analysis and Machine Intelligence*, **35**(3), 669–681.
- Park, C., Woehl, T.J., Evans, J.E. and Browning, N.D. (2015) Minimum cost multi-way data association for optimizing multitarget tracking of interacting objects. *IEEE Transactions on Pattern Analysis and Machine Intelligence*, **37**(3), 611–624.
- Qian, Y., Huang, J.Z., Li, X. and Ding, Y. (2016) Robust nanoparticles detection from noisy background by fusing complementary image information. *IEEE Transactions on Image Processing*, **25**(12), 5713–5726.
- Ribeiro, C., Lee, E.J., Longo, E. and Leite, E.R. (2005) A kinetic model to describe nanocrystal growth by the oriented attachment mechanism. *ChemPhysChem*, **6**(4), 690–696.
- Runger, G.C., Willemain, T.R. and Prabhu, S. (1995) Average run lengths for CUSUM control charts applied to residuals. *Communications in Statistics-Theory and Methods*, **24**(1), 273–282.
- Schwarz, G. (1978) Estimating the dimension of a model. *The Annals of Statistics*, **6**(2), 461–464.
- Sholl, D.S. and Skodje, R.T. (1996) Late-stage coarsening of adlayers by dynamic cluster coalescence. *Physica A: Statistical Mechanics and Its Applications*, **231**(4), 631–647.
- Simonsen, S.B., Chorkendorff, I., Dahl, S., Skoglundh, M., Sehested, J. and Helveg, S. (2010) Direct observations of oxygen-induced platinum nanoparticle ripening studied by in situ TEM. *Journal of the American Chemical Society*, **132**(23), 7968–7975.
- Voorhees, P.W. (1985) The theory of Ostwald ripening. *Journal of Statistical Physics*, **38**(1–2), 231–252.
- Wang, F., Richards, V., Shields, S. and Buhro, W. (2013) Kinetics and mechanisms of aggregative nanocrystal growth. *Chemistry of Materials*, **26**(1), 5–21.
- Woehl, T.J., Park, C., Evans, J.E., Arslan, I., Ristenpart, W.D. and Browning, N.D. (2013) Direct observation of aggregative nanoparticle growth: Kinetic modeling of the size distribution and growth rate. *Nano Letters*, **14**(1), 373–378.
- Xue, X., Penn, R.L., Leite, E.R., Huang, F. and Lin, Z. (2014) Crystal growth by oriented attachment: Kinetic models and control factors. *Crystal Engineering Communications*, **16**(8), 1419–1429.
- Yang, H.-G. and Zeng, H.-C. (2004) Preparation of hollow anatase TiO₂ nanospheres via Ostwald ripening. *The Journal of Physical Chemistry B*, **108**(11), 3492–3495.
- Yao, Y.-C. (1988) Estimating the number of change-points via Schwarz's criterion. *Statistics & Probability Letters*, **6**(3), 181–189.
- Zamba, K. and Hawkins, D.M. (2006) A multivariate change-point model for statistical process control. *Technometrics*, **48**(4), 539–549.
- Zhang, J., Huang, F. and Lin, Z. (2010) Progress of nanocrystalline growth kinetics based on oriented attachment. *Nanoscale*, **2**(1), 18–34.
- Zheng, H., Smith, R.K., Jun, Y.W., Kisielowski, C., Dahmen, U. and Alivisatos, A.P. (2009) Observation of single colloidal platinum nanocrystal growth trajectories. *Science*, **324**(5932), 1309–1312.

Appendix: Optimization of density estimation

We proposed to maximize the penalized log likelihood of the density functions by ADMM (Boyd *et al.*, 2011). We write the corresponding augmented Lagrangian as

$$L_{\rho}(\{a_{jt}\}, \{z_{jt}\}, \{c_{it}\}) = \sum_{t=1}^T L_t(\{a_{jt}\}) - (\lambda_2/2) \sum_{j=1}^n \sum_{t=1}^{T-1} (\Delta_2 z_{jt})^2 - \rho \sum_{t=1}^T \sum_{j=1}^n c_{jt} (a_{jt} - z_{jt}) - (\rho/2) \sum_{t=1}^T \sum_{j=1}^n (a_{jt} - z_{jt})^2, \quad (A1)$$

where

$$L_t(\{a_{jt}\}) = \sum_{i=1}^m y_{it} \eta_{it} - \sum_{i=1}^m \exp(\eta_{it}) - \lambda_1 \sum_{j=1}^{n-1} \frac{(\Delta_1 a_{jt})^2}{2}. \quad (A2)$$

The ADMM algorithm targets to find the saddle point of Equation [8], defined as

$$(\{\hat{a}_{jt}\}, \{\hat{z}_{jt}\}, \{\hat{c}_{it}\}) = \arg \min_{\{c_{it}\}} \max_{\{a_{jt}\}, \{z_{jt}\}} L_{\rho}, \quad (A3)$$

where $\{\hat{a}_{jt}\}$ is the maximizer of the penalized log likelihood of the density functions.

The saddle point is found by using the coordinate descent method Luenberger (1973). First we change the min-max problem to a max-min one by adding a negative sign in Equation (8) and rewriting it in a matrix form:

$$L'_{\rho}(A, Z, C) = - \sum_{t=1}^T L_t(A) + (\lambda_2/2) \sum_{j=1}^n \sum_{t=1}^{T-1} (\Delta_2 z_{jt})^2 + \rho C^T (A - Z) + (\rho/2) \sum_{t=1}^T \|A - Z\|_2^2, \quad (A4)$$

where $(A)_{jt} = a_{jt}$, $(Z)_{jt} = z_{jt}$, and $(C)_{jt} = c_{jt}$. Then we update A , Z , C iteratively to obtain the saddle point. When updating

one of the three variables, we fix the other two. The values of variables in the q th iteration are signified via the (q) superscript.

To update A , we solve

$$\arg \min_A - \sum_{t=1}^T L_t(A) + (\rho/2) \|A - Z^{(q)} + C^{(q)}\|_2^2. \quad (\text{A5})$$

The problem can be decomposed into T independent subproblems for each time t . Denote the t th column of A , Z , and C by a_t , z_t , and c_t , respectively. The difference operator Δ_1 can be rewritten as a matrix multiplication:

$$\sum_{j=1}^{n-1} (\Delta_1 a_{jt})^2 = a_t' D_1' D_1 a_t, \quad (\text{A6})$$

where D_1 is an $n \times n$ matrix with $(D_1)_{jj}$ as -1 , $(D_1)_{j(j-1)}$ as 1 , for $j = 2, \dots, n$, and all other elements being zero.

We can update a_t by

$$a_t^{(q+1)} = \arg \min_{a_t} \left\{ - \sum_{i=1}^m y_{it} \eta_{it} + \sum_{i=1}^m \exp(\eta_{it}) + (\lambda_1/2) a_t' D_1' D_1 a_t + (\rho/2) \left[a_t' a_t - 2 \left(z_t^{(q)} - c_t^{(q)} \right)' a_t \right] \right\}. \quad (\text{A7})$$

The solution procedure of the above minimization problem can follow Eilers and Marx (1996), as they solved a similar problem. However, we need to make some modification to the approach of Eilers and Marx (1996), as we included a new term (the fourth term in the large bracket) in the above objective function. According to Eilers and Marx (1996), the solution of a_t consists in the first derivative of the above objective function to zero. That leads us to the following equation:

$$B_t^+ - B' \exp(Ba_t) = \lambda_1 D_1' D_1 a_t + \rho \left[a_t - \left(z_t^{(q)} - c_t^{(q)} \right) \right], \quad (\text{A8})$$

where $B_t^+ = [B_{1t}^+, \dots, B_{mt}^+]'$ and $B_{jt}^+ = \sum_s B_j(\phi_{st})$. Unfortunately, the above equation does not have a closed-form solution for a_t , so we have to solve it through an iterative procedure by using the following equation (which is a first-order Taylor

expansion of the exponential term, so that a_t can be solved through a weighted linear regression):

$$B_t^+ - B' \exp(B\hat{a}_t) + B' B \hat{a}_t + \rho \left(z_t^{(q)} - c_t^{(q)} \right) = [B'B + \lambda_1 D_1' D_1 + \rho I_n] a_t, \quad (\text{A9})$$

where I_n is the $n \times n$ identity matrix and \hat{a}_t is the estimate from the previous iteration, whose initial value is set to be $a_t^{(q)}$ (from the q th step). Once the numerical iterative procedure converges, the resulting a_t is treated as $a_t^{(q+1)}$.

To update Z , we solve

$$Z^{(q+1)} = \arg \min_Z \left\{ \lambda_2 \sum_{j=1}^n \sum_{t=1}^{T-1} (\Delta_2 z_{jt})^2 + (\rho/2) \|A^{(q+1)} - Z + C^{(q)}\|_2^2 \right\}. \quad (\text{A10})$$

The terms in the large bracket can be rewritten as

$$\|A^{(q+1)} - Z + C^{(q)}\|_2^2 + \frac{\lambda_2}{\rho} \sum_{j=1}^n \sum_{t=1}^{T-1} (\Delta_2 z_{jt})^2. \quad (\text{A11})$$

The second term can be transformed into a matrix form:

$$\sum_{j=1}^n \sum_{t=1}^{T-1} (\Delta_2 z_{jt})^2 = \|ZD_2\|_2^2, \quad (\text{A12})$$

where D_2 is a $T \times T$ matrix with $(D_2)_{tt}$ as -1 , $(D_2)_{t(t+1)}$ as 1 , for $t = 1, \dots, T-1$, and all other elements being zero. In fact, the above minimization problem has a closed-form solution for $Z^{(q+1)}$, which is

$$Z^{(q+1)} = [A^{(q+1)} + C^{(q)}] \left(I_T + \frac{\lambda_2}{\rho} D_2 D_2' \right)^{(-1)}. \quad (\text{A13})$$

Finally, we update the Lagrangian multipliers C by

$$C^{(q+1)} = C^{(q)} + (A^{(q+1)} - Z^{(q+1)}). \quad (\text{A14})$$

We continue the iteration until all of these variables converge.